JOURNAL OF THERMOPHYSICS AND HEAT TRANSFER
Vol. 24, No. 2, April–June 2010

Analysis of a Cylindrical Specimen Heated by an Impinging Hot Hydrogen Jet

Ten-See Wang,* Van Luong,† John Foote,‡ and Ron Litchford§
NASA Marshall Space Flight Center, Huntsville, Alabama 35812
and
Yen-Sen Chen¶
National Space Organization, Hsinchu 30078, Taiwan, Republic of China

DOI: 10.2514/1.47737

A computational conjugate heat transfer methodology was developed to study the heat transfer inside a cylindrical specimen heated by an impinging hot hydrogen jet for nuclear thermal propulsion applications. The development involved the implementation of a time-marching solid conduction heat transfer procedure onto a transient pressure-based unstructured-grid computational-fluid-dynamics formulation. The conjugate heat transfer between the solid and the gaseous media were anchored with a standard solid heat transfer code. Three steady-state and five transient analyses were then conducted, using thermal conductivities representing three hypothetical composite materials. It was found that material thermal conductivity strongly influences the heat transfer characteristics. In addition, it was observed that during steady-state operations, the specimen experiences a high temperature but a low thermal gradient, whereas during transient operations, the specimen undergoes a high thermal gradient during the initial heating. It was also found from the transient analyses that the shorter the ramp time, the stronger the thermal gradient is experienced by the cylindrical specimen.

Nomenclature

C_p	=	heat capacity
C_1, C_2, C_3, C_μ	=	turbulence modeling constants, 1.15, 1.9, 0.25, and 0.09.
D	=	diffusivity
H	=	total enthalpy
K	=	thermal conductivity
k	=	turbulent kinetic energy
p	=	pressure
Q	=	heat flux or heat source
T	=	temperature
t	=	time, s
u_i	=	mean velocities in three directions
x	=	Cartesian coordinates
ε	=	turbulent kinetic energy dissipation rate
μ	=	viscosity
μ_t	=	turbulent eddy viscosity, $\rho C_\mu k^2/\varepsilon$
Π	=	turbulent kinetic energy production
ρ	=	density
σ	=	turbulence modeling constants
τ	=	shear stress
ω	=	chemical species production rate

Subscripts

cl	=	centerline
s	=	surface
t	=	turbulent flow
v	=	volume
0	=	cells at the fluid/solid interface
1	=	cells at one point into the solid

Superscript

$'$	=	next time level solution

I. Introduction

NUCLEAR thermal propulsion (NTP) may open up the solar system to far broader and faster exploration than is now possible with chemical propulsion. The feasibility of solid-core NTP systems was established by extensive testing in the Rover/NERVA (Nuclear Engine for Rocket Vehicle Application) programs and the technical merits of NTP have been identified and summarized [1,2]. The basic concept involves a reactor core consisting of several hundred flow elements that are used to heat a low-molecular-weight gas, such as hydrogen. Thrust is generated as the hot hydrogen expands through a high-expansion-ratio nozzle. However, the need to push the flow element temperature to extremes in order to maximize performance intensifies the possibility of material failures [3]. For example, the midsection corrosion was named after the unexpected mass loss of materials at the midsection of the flow element due to coating cracks, which was speculated to have been caused by large temperature gradients generated during operation or by radiation damage [3]. Therefore, improving the thermal stress resistance of the flow element material is a high priority for nuclear thermal engine development.

To develop candidate high-temperature materials that will be compatible with the hot hydrogen environment of a high performance solid-core NTP engine, new materials for the flow elements must be developed, screened, and tested. Simultaneously, an accompanying computational methodology must be developed for analysis of test results in order to understand the failure mechanism and develop steps for improving the thermal resistance of the materials and/or operating procedures.

Presented as Paper 2926 at the 9th AIAA/ASME Joint Thermophysics and Heat Transfer Conference, San Francisco, CA, 5–8 June 2006; received 27 October 2009; revision received 22 December 2009; accepted for publication 23 December 2009.

*Task Manager, Mail Stop ER42, Fluid Dynamics Branch. Senior Member AIAA.
†Project Engineer, Mail Stop ER43, Thermal and Combustion Analysis Branch.
‡Project Engineer, Mail Stop ER32, Combustion Devices Design and Development Branch.
§Task Manager, Mail Stop ER32, Combustion Devices Design and Development Branch. Associate Fellow AIAA.
¶Senior Research Fellow. Senior Member AIAA.

As a starting point, a nonnuclear materials tester for hot hydrogen exposure of nuclear thermal rocket materials was being developed in an arc heater facility [4]. The tester consists of a shielded and water-cooled chamber, inside which a cylindrical specimen will be heated with an impinging hot hydrogen jet coming from an arc heater while the performance of the specimen during heating is monitored by instruments in two optical ports. As a parallel effort, this study describes the development of a computational conjugate heat transfer methodology that can simulate the detailed heat transfer characteristics of the specimen inside the materials tester, thereby providing necessary flow and heat transfer properties for analysis of the test results in the future. The computational methodology development is achieved by implementing a solid heat transfer analysis onto an existing computational fluid dynamics (CFD) methodology: UNIC, which has been heavily benchmarked on various flow and gaseous heat transfer applications, except for those of conjugate heat transfers. The anchoring of the conjugate heat transfer of the new implementation is described in this paper. It is achieved by modeling a cylindrical specimen heated by an impinging hot hydrogen jet inside the aforementioned materials tester [4] and by comparing the results with those of a standard solid heat transfer code, with three constant thermal conductivities that cover the possible range of potential flow element materials. After the benchmarking of the new implementation, the UNIC code is then applied to a series of steady-state and transient analyses, with variable thermal conductivities reported for three hypothetical nuclear composite materials [3] to simulate the heat transfer characteristics of a cylindrical specimen being heated by an impinging hot hydrogen jet with material properties potentially close to what might be tested in the future. The transient computations conducted include impulsive 10 and 50 s ramp starts of the hot hydrogen jet. The results of the numerical tests are reported and discussed.

II. UNIC Computational Methodology

A. Computational Fluid Dynamics and Gas-Side Heat Transfer

The computational methodology is based on a multidimensional finite-volume viscous, chemically reacting, unstructured-grid pressure-based formulation. Time-varying transport equations of continuity, species continuity, momentum, total enthalpy, turbulent kinetic energy, and turbulent kinetic energy dissipation rate were solved using a time-marching subiteration scheme and are written as:

$$\frac{\partial \rho}{\partial t} + \frac{\partial}{\partial x_j}(\rho u_j) = 0 \tag{1}$$

$$\frac{\partial \rho \alpha_i}{\partial t} + \frac{\partial}{\partial x_j}(\rho u_j \alpha_j) = \frac{\partial}{\partial x_j}\left[\left(\rho D + \frac{\mu_t}{\sigma_\alpha}\right)\frac{\partial \alpha_i}{\partial x_j}\right] + \omega_i \tag{2}$$

$$\frac{\partial \rho u_i}{\partial t} + \frac{\partial}{\partial x_j}(\rho u_j u_i) = -\frac{\partial p}{\partial x_i} + \frac{\partial \tau_{ij}}{\partial x_j} \tag{3}$$

$$\begin{aligned}\frac{\partial \rho H}{\partial t} + \frac{\partial}{\partial x_j}(\rho u_j H) &= \frac{\partial p}{\partial t} + Q_r + \frac{\partial}{\partial x_j}\left[\left(\frac{K}{C_p} + \frac{\mu_t}{\sigma_H}\right)\nabla H\right] \\ &+ \frac{\partial}{\partial x_j}\left\{\left[(\mu + \mu_t) - \left(\frac{K}{C_p} + \frac{\mu_t}{\sigma_H}\right)\right]\nabla \frac{V^2}{2}\right\} \\ &+ \frac{\partial}{\partial x_j}\left[\left(\frac{K}{C_p} + \frac{\mu_t}{\sigma_H}\right)\left(u_k \frac{\partial u_j}{\partial x_k} - \frac{2}{3} u_j \frac{\partial u_k}{\partial x_k}\right)\right]\end{aligned} \tag{4}$$

$$\frac{\partial \rho k}{\partial t} + \frac{\partial}{\partial x_j}(\rho u_j k) = \frac{\partial}{\partial x_j}\left[\left(\mu + \frac{\mu_t}{\sigma_k}\right)\frac{\partial k}{\partial x_j}\right] + \rho(\Pi - \varepsilon) \tag{5}$$

$$\begin{aligned}\frac{\partial \rho \varepsilon}{\partial t} + \frac{\partial}{\partial x_j}(\rho u_j \varepsilon) &= \frac{\partial}{\partial x_j}\left[\left(\mu + \frac{\mu_t}{\sigma_\varepsilon}\right)\frac{\partial \varepsilon}{\partial x_j}\right] \\ &+ \rho \frac{\varepsilon}{k}\left[C_1 \Pi - C_2 \varepsilon + \left(\frac{C_3 \Pi^2}{\varepsilon}\right)\right]\end{aligned} \tag{6}$$

A predictor–corrector solution algorithm was employed to provide coupling of the governing equations. A second-order central-difference scheme was employed to discretize the diffusion fluxes and source terms. For the convective terms, a second-order upwind total-variation-diminishing difference scheme was used. To enhance the temporal accuracy, a second-order backward difference scheme was employed to discretize the temporal terms. Details of the numerical algorithm can be found in [5–9].

An extended k–ε turbulence model [10] was used to describe the turbulence. A modified wall function approach was employed to provide wall boundary layer solutions that are less sensitive to the near-wall grid spacing. Consequently, the model has combined the advantages of both the integrated-to-the-wall approach and the conventional law-of-the-wall approach by incorporating a complete velocity profile and a universal temperature profile [8]. A two-species one-reaction mechanism, which is a subset of a kerosene combustion mechanism [11], was used to describe the hydrogen dissociation and recombination chemical kinetics.

As mentioned before, the gas-side computational methodology has been anchored in various flow and heat transfer applications. For example, the gas-side computational methodology has been used to compute the plasma created by laser heating, through which a detonation wave was generated to propel the laser lightcraft [7]. Thermophysics of plasma initiation, laser radiation, nonequilibrium plasma radiation, and plasma resonance were computed, and results of the coupling coefficient compared well with those of measurement. The convective and radiative wall heat fluxes of a liquid rocket engine thruster were computed and compared well with those of the tests and the design calculations [8]. The transient nozzle side load that is strongly influenced by wall heat transfer was computed and reported [9]. The computed peak side load and the shock breathing frequency compared well with those of engine hot-fire tests. Also, the computed radiative heat fluxes from an aerospike engine plume-induced base-heating environment compared well with those of engine hot-fire tests [12].

B. Computational Conjugate Heat Transfer in Solids

The solid heat conduction equation is solved with the gas-side heat flux distributions as its boundary conditions. The solid heat conduction equation can be written as

$$\frac{\partial \rho C_p T}{\partial t} - \frac{\partial}{\partial x_j}\left(K \frac{\partial T}{\partial x_i}\right) = Q_v + Q_s \tag{7}$$

where Q_v and Q_s represent source terms from volumetric and boundary contributions, respectively. The present conjugate heat transfer model solves the heat conduction equation for the solid blocks separately from the fluid equations. The interface temperature between the gas and the solid, which is stored at interior boundary points, is calculated using heat flux continuity condition. For solution stability and consistency, the gas and the solid interface boundary temperatures are updated using the transient heat conduction in Eq. (7). The heat conduction equation on the fluid–solid interface can be discretized as

$$\frac{1}{2}\rho C_p \frac{T_0' - T_0}{\Delta t} = \frac{1}{\Delta x_j}\left(K \frac{T_1 - T_0}{\Delta x_j} - Q_s\right) \tag{8}$$

where Q_s is the wall heat flux from the solid wall to the fluid, which has an opposite sign to that from the fluid to the solid. The $\frac{1}{2}$ factor on the left-hand side of the previous equation comes from the fact that only half of the solid cell is involved in the control volume. The following expression is obtained for updating the interface temperature:

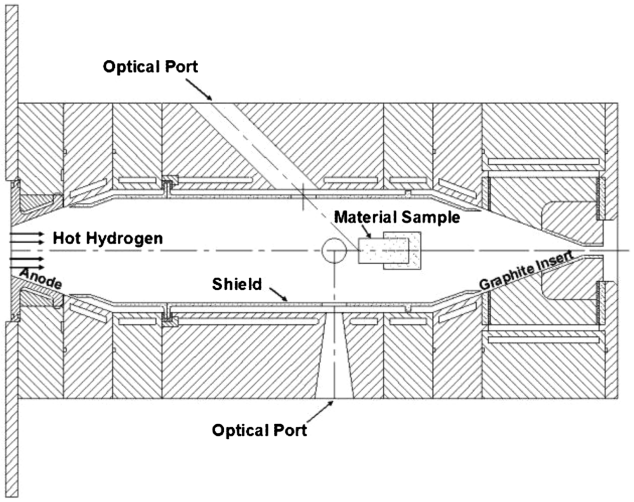

Fig. 1 Test apparatus.

$$T_0' = (1 - A)T_0 + AT_1 - BQ_s \tag{9}$$

where

$$A = \frac{2\Delta t K}{\rho C_p \Delta x_j^2} \tag{10}$$

$$B = \frac{2\Delta t}{\rho C_p \Delta x_j} \tag{11}$$

Because Eq. (8) is in transient form, it is applicable to transient applications. For steady-state solutions, the acceleration factor could be applied to force faster convergence of heat conduction in the solid. In this work, a multiplication factor of 10 is applied to A and B for steady-state solutions.

III. Nonnuclear Test Fixture Description

The cylindrical specimen to be analyzed is inserted in a sample holder and placed in a test fixture designed for new materials development and testing in a separate effort [4], as depicted in Fig. 1. The test fixture is directly mated to an arc heater (not shown) that provides hot hydrogen flow. Optical ports are fitted to allow real-time pyrometer and laser diagnostics measurements for material surface temperature and centerline gas temperature, respectively. The copper test chamber is water cooled. A tungsten/rhenium shield, which serves as a convection shield and a radiation shield, allows the hot hydrogen jet to impinge on the specimen with maximum energy and minimum heat loss to the copper chamber. In this work, the computational domain includes all the of the flow area except for the arc heater and the cooling channels. The effects of the arc heater and the cooling channels were represented as inlet and wall boundary conditions with separate calculations. It is worth noting that the UNIC was used to help the designing of the test fixture. The current shield design was found to provide the lowest heat loss to the chamber wall and the highest hot-hydrogen-delivering temperature; thereby, it is superior to the baseline (without shield) and the funnel-shaped partial-shield designs. The computed total heat flux to the chamber wall was lower than the safety margin. Details of the design analyses are reported in [13].

IV. Computational Grid Generation

To analyze the thermophysics of a cylindrical specimen heated by an impinging hot hydrogen jet inside the materials tester, hybrid computational grids were generated using the software package GRIDGEN (Ver. 15.07, Pointwise, Inc., Ft. Worth, TX) [14]. Axisymmetric grids were used, assuming the flow was symmetric about the axial axis. A series of grid verification studies, using grid sizes ranging from 10,024, to 19,448, were performed to determine the current grid size (16,880) [13] for best solution. It was found during the grid study that the computed gas–solid interface temperature is most favorable when structured grid layers are present on both sides of the gas–solid interface. Figure 2 shows such a grid layout, in which structured (rectangular) cells are used for the specimen and the region surrounding it. Structured cells are also used near wall boundaries and for flow inlet and outlet boundaries, whereas the rest of the interior region is filled with unstructured (triangular) cells (mostly not shown). It can be seen from Fig. 2 that heat is being transferred from the impinging hot hydrogen jet to the specimen, and the computed specimen temperature contours exhibit approximately one-dimensional behavior.

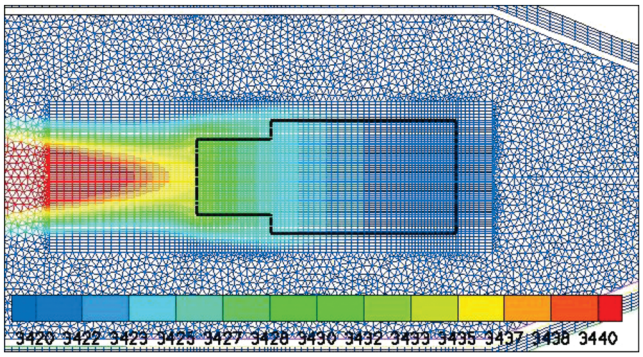

Fig. 2 Hybrid computational grid layout colored by typical computed temperature contours of hot hydrogen jet impinging on a rod-shaped specimen.

V. Boundary Conditions, Thermal Conductivities, and the Run Matrix

No-slip condition was applied to the solid walls. A fixed mass flow rate boundary condition was used at the hot hydrogen inlet, and a mass conservation boundary condition was used at the exit. The hot hydrogen entered the chamber at 3500 K. A fixed temperature of 400 K was estimated for the chamber wall, and the wall temperature of the shield facing the chamber wall was estimated to be 2600 K, through separate one-dimensional heat transfer calculations. An adiabatic condition was applied to the rest of the chamber walls [e.g., the flanges (that hold the shield) and the graphite insert (in the convergent section)]. The hydrogen inlet mass flow rate was 10 g/s, and the chamber pressure was 35 atm. A series of precalculations were performed to iterate the inlet temperature and the species concentrations, such that the inlet species concentrations corresponded to a state of temperature at 3500 K for a nominal operating condition.

Table 1 shows the run matrix for this study. Benchmark cases 1, 2, and 3 are steady-state runs with thermal conductivities of 50, 80, and 140 W/mK, respectively. These constant thermal conductivities cover the important range of thermal conductivities of potential composite materials. The following steady-state and transient simulation cases used variable thermal conductivities reported for composite materials [3]. Simulation cases 1, 2, and 3 are steady-state runs, whereas simulation cases 4, 5, and 6 are impulsive start runs, simulation case 7 is a 10 s ramp start run, and simulation case 8 is a

Table 1 Run matrix

Case	State	K
Benchmark 1	Steady	50
Benchmark 2	Steady	80
Benchmark 3	Steady	140
Simulation 1	Steady	Composite A
Simulation 2	Steady	Composite B
Simulation 3	Steady	Irradiated composite B
Simulation 4	Impulsive start	Composite A
Simulation 5	Impulsive start	Composite B
Simulation 6	Impulsive start	Irradiated composite B
Simulation 7	10 s ramp start	Composite B
Simulation 8	50 s ramp start	Composite B

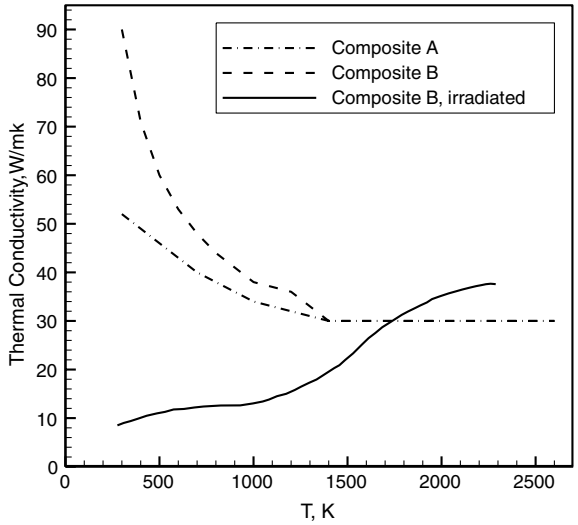

Fig. 3 Variable thermal conductivities for three specimens.

50 s ramp start run. By using the thermal conductivities of the hypothetical composite materials, named as composites A and B and irradiated composite B, we can gain some insight of their thermal behaviors that may help future composite material development. The irradiated composite B is composite B material after the test. The thermal conductivities of these specimens as a function of the temperatures [3] are shown in Fig. 3. It can be seen that composite B has a higher thermal conductivity than that of composite A, when the temperature is less than 1400 K. In fact, composite B has the highest thermal conductivity that can be achieved for the carbide composite that still retains desirable mechanical properties during the time of testing [3]. In contrast, the thermal conductivity of the irradiated composite B is much lower than the unirradiated composite B in the low temperatures. The reason for which was speculated as a result of annealing. Finally, as temperatures exceed about 1600 K, the thermal conductivity of all three composites seems to converge to values between $30 \sim 40$ W/mK and that of the irradiated composite B is the highest one at about 40 W/mK.

VI. Results and Discussion

Figure 4 shows the typical computed temperature, H (atom) concentration contours, and streamlines simulating nominal steady-state test conditions for the entire computational domain. It can be seen from the temperature contours that the entire thrust chamber is almost uniformly heated, except for the region between the shield and the water-cooled chamber wall. This is because the shield serves as both the convection and the radiation shields that protect the chamber wall from the convective heating of the hot hydrogen flow and from the radiative heating of the hot specimen. Nevertheless, there is still some minor heat loss to the environment, hence the hot hydrogen jet temperature drops slightly as it impinges and wraps around the material specimen. As the local temperature decreases, H (atom) recombines to become H_2 (molecule). This is shown in the middle H contours, in which its concentration decreases as the hot jet approaches the sample. It should be noted that the hydrogen dissociation and recombination reactions are highly correlated with the local temperature and are very important in the accurate prediction of the entire chamber thermo-flowfield [13]. It is also noted that between the two additive convective and radiative heat transfer mechanisms, the chamber wall heat flux contribution from the convective heating of the hot hydrogen jet is about 2.5 times higher than that of the radiative heating from the hot specimen [13].

The computed streamlines at the bottom of Fig. 4 show an expanding hot hydrogen jet impinging on and flowing around the specimen and eventually exhausting into the convergent exit section. A large recirculation zone appears in the divergent section of the chamber, near the entrance, whereas a small recirculation region forms behind the sample holder; both of which are strongly affected by the turbulence. Note, although, the plots show a distinctively strong hot hydrogen jet and two recirculated flow regions: the pressure and Mach number contours are fairly uniform inside the chamber (not shown) due to the largely low subsonic flowfield and the protection of the shield. The flow becomes supersonic in the exit pipe.

A. Steady-State Benchmark Analysis with Constant Thermal Properties

Figure 5 shows a comparison of the computed steady-state centerline coupon (specimen) temperatures, using conjugate heat transfer methodology developed in this work with those obtained from the separate conduction heat transfer code SINDA (Systems Improved Numerical Differencing Analyzer) [15]. SINDA is a standard solid heat transfer code that is capable of solving the heat transfer inside a solid body, such as the cylindrical coupon in question, as long as the boundary condition of the solid-body surface is given. In this case, the boundary condition of the solid surface is the heat flux at the gas–solid interface, which can be obtained from the gas-side CFD solutions. In practice, in order to solve the heat transfer inside the cylindrical specimen, SINDA needs to iterate on the solid domain with at least three CFD solutions at three different fixed solid surface temperatures as inputs for the first and follow-up iterations. The range of the three different solid temperatures of the first iteration has

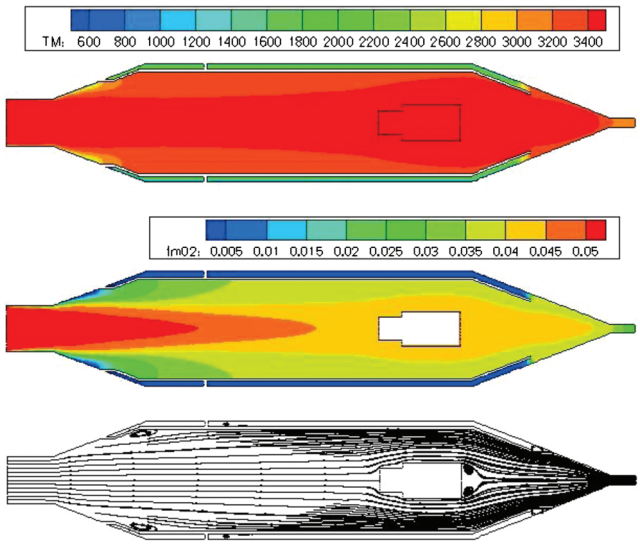

Fig. 4 From top to bottom, typical computed steady-state temperature and H mass fraction contours and streamlines.

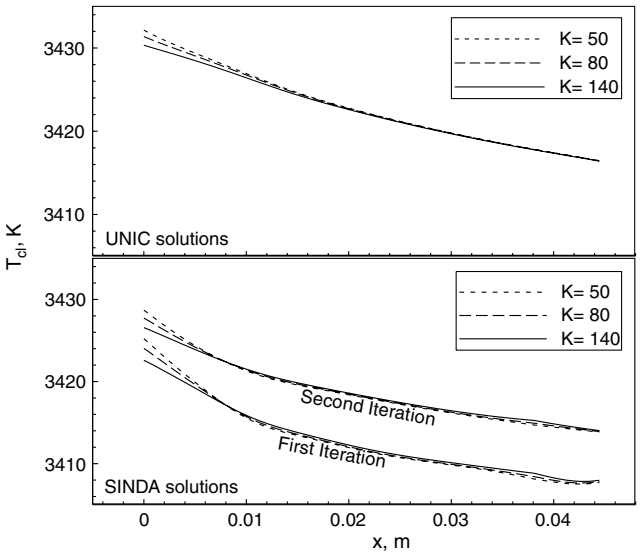

Fig. 5 A comparison of computed steady-state centerline specimen temperatures.

to be large enough to cover the final surface temperatures. After the first iteration, the improved gas–solid interface temperatures from SINDA will provide a better guide for the next three interface temperatures for the CFD to solve, and the iterations repeat themselves until convergence. The SINDA code is therefore a useful tool to benchmark the solid heat transfer part of the newly added conjugate heat transfer facility of the UNIC code when test data are not yet available. Other than CFD-computed heat flux at the gas–solid interface, the solid surface temperature, the offwall point temperatures, and the heat transfer coefficients from the CFD solutions can also be used as inputs for SINDA iterations.

In the steady-state benchmark cases, CFD solutions using three constant thermal conductivities (50, 80, and 140 W/mK) measured at room temperature for flow element materials that were heat treated at 2800, 3050, and 3120 K, respectively [3], were performed. In each constant thermal conductivity case, three CFD solutions were performed on three arbitrarily chosen wall temperatures of 300, 2500, and 3400 K, as guesses for the first SINDA iteration. It should be noted that these three fixed wall temperatures imply that three wall heat flux profiles were imposed on the gas–solid interface. As an example, the first SINDA solution for the case of a constant thermal conductivity of 50 narrows the wall temperature range from the initial guess of $300 \sim 3400$ K to that of a very narrow $3406 \sim 3412$ K. Three more CFD solutions were then performed at three wall temperatures of 3405, 3410, and 3413 K, and the solutions of the offwall temperatures and the heat transfer coefficients were then fed to SINDA for the second iteration. For all three thermal conductivity cases, only two SINDA iterations were needed to reach convergence.

It can be seen from Fig. 5 that the UNIC-computed centerline temperatures already compared reasonably well with those obtained from the first SINDA iteration, although the maximum deviation is less than 10 K. And the CFD-computed centerline temperatures compared even better with those of the second SINDA iteration; this time, the maximum deviation was less than 3 K. In summary, Fig. 5 demonstrates that the UNIC-computed solid temperatures compare very well with those of the standard solid heat transfer code SINDA. Both UNIC and SINDA solutions exhibit a similar trend. For example, high thermal gradients occur near the stagnation point ($x = 0$). In addition, the lowest thermal conductivity ($k = 50$) gives the highest thermal gradient, whereas the highest thermal conductivity ($K = 140$) results in the lowest thermal gradient.

B. Steady-State Analysis with Variable Thermal Properties

For benchmark purposes, solutions for three constant thermal conductivities were performed, as mentioned previously. For actual nuclear flow element materials, such as composite A, composite B, and irradiated composite B, their thermal conductivities vary with the temperatures, as shown in Fig. 3. To simulate the behaviors of the actual flow element materials, analyses with those variable thermal conductivities were performed. Figure 6 shows the computed steady-state centerline temperatures for these three specimens, simulated as cylindrical pellets that are heated by hot hydrogen jet impingement, as described in Fig. 1. It can be seen that the centerline temperature profiles for composite A and composite B overlap, whereas that for the irradiated composite B deviates with those of composite A and composite B only slightly near the stagnation point ($x = 0$) and near $x = 0.04$. This is because the cylindrical pellet is surrounded by hot hydrogen flow, and the whole pellet is heated to temperatures from about 3400 to 3425 K, as shown in Fig. 4. At these temperature levels, the thermal conductivities are nearly constant ($30 \sim 38$ W/mK); note that those of the irradiated composite B converge to the highest value at 38 among the three, as shown in Fig. 3.

Although it appears that there are some temperature gradients for the curves in Fig. 6, in actuality, the steady-state thermal gradients for all three specimens are rather benign, because the temperature range is narrow. That means there is no meaningful thermal gradient or high thermal stress for these pellets during the steady-state heating with the current set up. On the other hand, it has been shown that certain detrimental physics for rocket engines, such as nozzle side loads, only happen during the transient startup or shutdown process and never in the steady-state process [9]. With the range of thermal conductivities shown in Fig. 3, it is speculated that the stronger thermal gradients could occur during the transient startup of the impingement heating process. That possibility is investigated by performing three impulsive and two linear ramp startup computations, as discussed in the following section.

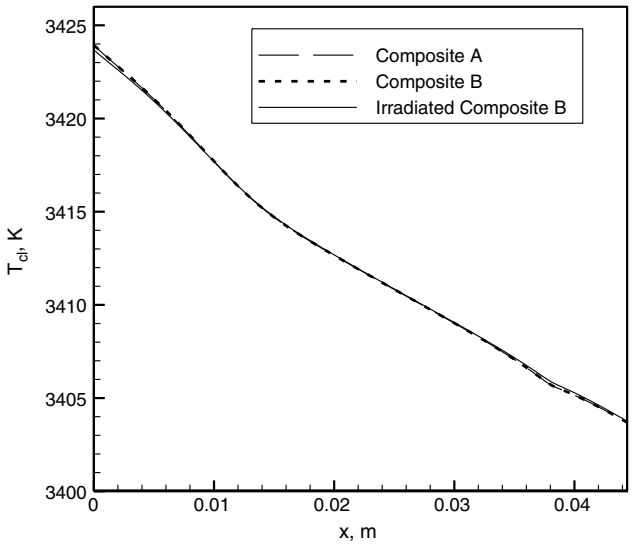

Fig. 6 Computed steady-state centerline temperatures for three hypothetical specimens.

C. Transient Analysis: Impulsive Starts with Variable Thermal Properties

Three impulsively started transient conjugate heat transfer computations were performed for the three specimens (composite A, composite B, and irradiated composite B), with the variable thermal conductivities as described in Fig. 3. Hydrogen gas was assumed to be in the tester initially at the temperature and pressure of 300 K and 1 atm, respectively. The initial pellet temperature was assumed to be at 300 K. For the most conservative case, hot hydrogen was assumed to enter the tester impulsively at 3500 K and 35 atm, meaning the inlet hydrogen gas was heated to 3500 K and pressurized to 35 atm instantly by the arc heater at time zero.

As mentioned in the last section, it was speculated that impulsive start up of the impingement heating could create high thermal gradient or thermal shock in the solids. Figure 7 shows the computed transient specimen centerline temperature profiles for composite A.

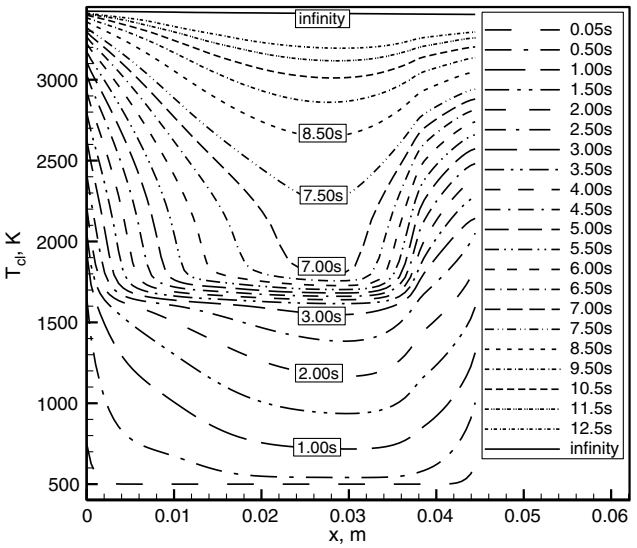

Fig. 7 Computed cylindrical specimen centerline temperature history for composite A during an impulsive start.

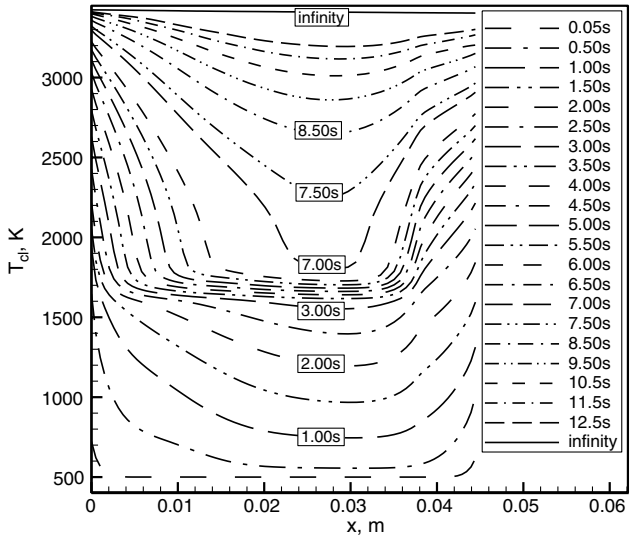

Fig. 8 Computed cylindrical specimen centerline temperature history for composite B during an impulsive start.

It can be seen that, unlike the steady-state profile, strong thermal gradients occur at both ends of the pellet where the impingement end or the stagnation point end ($x = 0$) encounters the strongest thermal gradient throughout most of the transient heating process, especially during the 3 to 7 s period. During that time period, it can be seen that the center core had a difficult time getting heated up from 1600 to 1800 K, resulting in strong thermal gradients at the two ends. This phenomenon is strongly correlated to the low thermal conductivity at high temperatures for composite A, as shown in Fig. 3.

Figures 8 and 9 show the computed transient temperature profiles for composite B and irradiated composite B, respectively. It can be seen that, except in the early heating period ($0.05 \sim 1.5$ s) when the irradiated composite B shows a stronger thermal gradient than that of composite B, both show similarly strong thermal gradients at the two ends of the cylindrical pellet when the central core reaches 1600 K. In fact, during that time period, the transient temperature profiles of composite B and irradiated composite B look qualitatively similar to those of composite A (Fig. 7).

The similarity in the occurrence of the high thermal gradient during the $3 \sim 7$ s time period for composites A and B and irradiated composite B correlates to the fact that the thermal conductivity of all three specimens converges to similarly low values as temperatures exceed 1,600 K, even though their individual thermal conductivity profiles look quite different in lower temperatures. Figures 7–9 demonstrate that the thermal wave propagation inside the cylindrical pellet is a strong function of the characteristics of the thermal conductivity. In addition, it could be inferred that, for other specimens with completely different thermal conductivity characteristics, different thermal transient histories may have been computed. Therefore, the thermal stress resistance may be improved by increasing the thermal conductivity through a carefully controlled heat treatment process for composite materials. The results from Figs. 7–9 also show that, for the three cylindrical flow element specimens studied, it takes more than 12.5 s to heat the pellets up, using impulsive starts.

D. Transient Analysis: 10 and 50 s Ramp Starts with Variable Thermal Properties

The 10 s ramp start assumes the hydrogen gas inlet temperature and pressure are brought up linearly to 3,500 K and 35 atm from 300 K and 1 atm, respectively, during a 10 s period. This means that the leading edge of the cylindrical pellet does not see the final temperature until the 10th second, when compared to sensing the final temperature at the start command of the impulsive start. Only the effect of the thermal conductivity characteristics of composite B was investigated, because the impulsive start analyses show that the

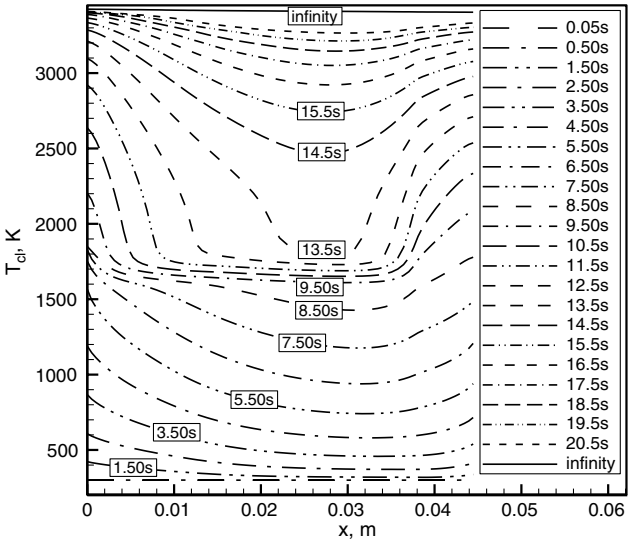

Fig. 10 Computed cylindrical specimen centerline temperature history for composite B during a 10 s ramp start.

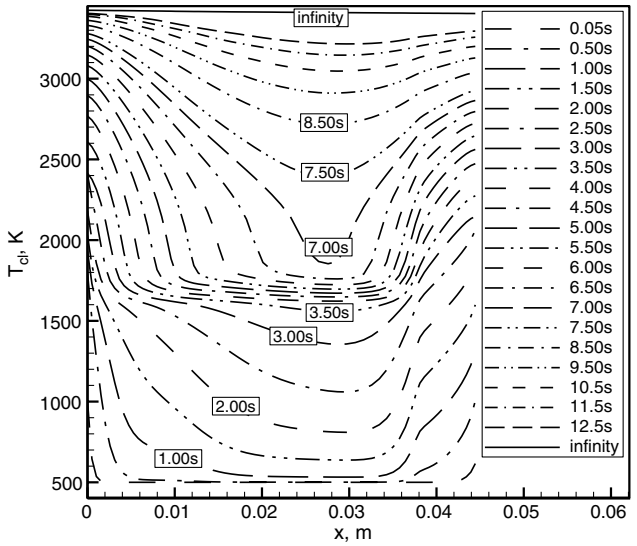

Fig. 9 Computed cylindrical specimen centerline temperature history for irradiated composite B during an impulsive start.

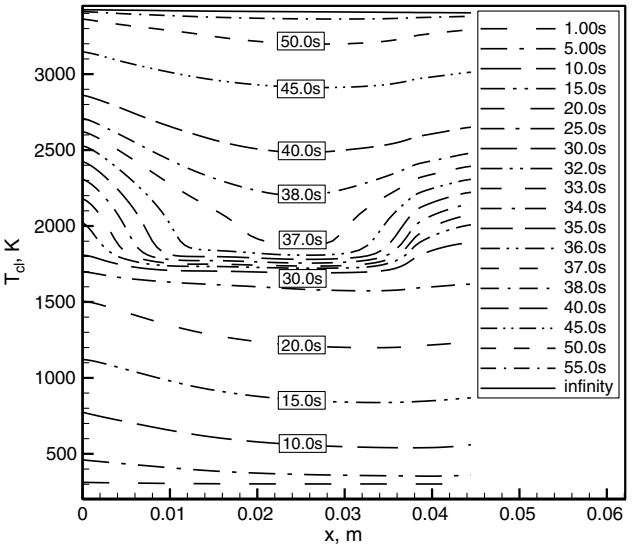

Fig. 11 Computed cylindrical specimen centerline temperature history for composite B during a 50 s ramp start.

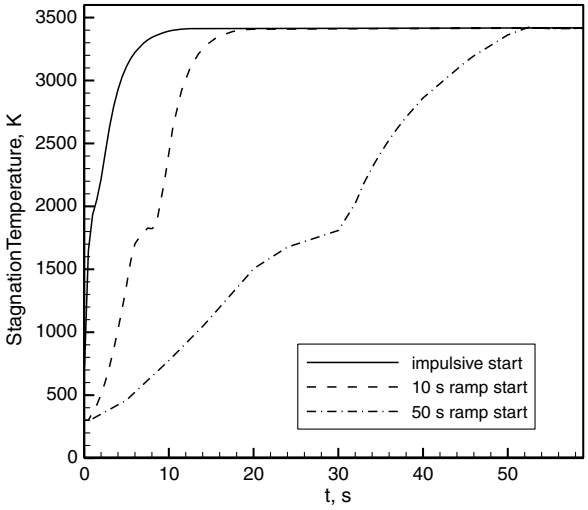

Fig. 12 Computed cylindrical specimen stagnation temperature histories for composite B.

transient behaviors of all three specimens are similar at high temperatures. Figure 10 shows the computed transient centerline temperature history for composite B during the 10 s ramp start. It can be seen that, from 0.05 to 8.5 s, the thermal gradients are fairly benign at both ends of the cylindrical pellet when compared to those of the impulsive starts. At 9.5 s, or as the center core temperature reaches 1,600 K, higher thermal gradients again start to show. Hence, the thermal conductivity effect from Fig. 3 still dominates in the 10 s ramp start, even though the high thermal gradient occurs later than those of the impulsive starts. Note the total heat-up time for the cylindrical pellet is now more than 20.5 s.

Similarly, Fig. 11 shows the computed transient centerline temperature history for composite B during a 50 s ramp start. In this case, high thermal gradients begin at about 30 s, whereas the total heat-up time for the specimen now exceeds 50 s. Comparing the transient heating profiles of Figs. 8, 10, and 11, it can be concluded that the longer the heating time, the weaker the thermal gradient in the pellet. Furthermore, similar conclusions can be reached by plotting the computed cylindrical specimen stagnation temperature histories against the elapsed time for composite B, as shown in Fig. 12. Again, it can be seen that the longer the ramp time, the longer it takes for the stagnation temperature to reach the final temperature. And the longer the ramp time, the lower the thermal gradient will be. The results of the transient analyses demonstrate that thermal conductivity controls the thermal gradient in the cylindrical specimen during the transient operations, and the transient heating process could be a factor when considering scenarios that affect the integrity of the flow element material during testing.

VII. Conclusions

A computational conjugate heat transfer methodology was developed to study the heat transfer from a hot hydrogen jet impinging on a cylindrical pellet made of hypothetical materials. This is accomplished by implementing a solid heat transfer procedure onto an existing CFD formulation. The solid heat transfer module was anchored by comparing the computed steady-state pellet centerline temperatures with those obtained from a standard solid heat transfer code with three representative, constant thermal conductivities. More analyses were then performed for hypothetical cylindrical pellets, using variable thermal conductivities. Under the assumptions made in this study, high temperatures were computed throughout the entire specimen during the steady-state heating, whereas high thermal gradients were obtained during the transient heating processes. During the transient heating processes, high thermal gradients occurred at both ends of the pellet, especially near the impingement point. The transient heating behavior inside those rod-shaped specimens depends strongly on their thermal conductivity characteristics and heating rates. It is determined that both steady-state and transient heating processes are important, because both the high temperature and high thermal gradient could affect the integrity of a specimen under testing conditions.

Acknowledgments

This study was partially supported by a Nuclear Systems Office task entitled, "Multiphysics Thrust Chamber Modeling" and by a Marshall Space Flight Center (MSFC) Internal Research and Development focus area task entitled, "Hot-Hydrogen Materials and Component Development." Ron Porter was the Marshall Space Flight Center Nuclear Systems Office Manager. Wayne Bordelon was the Nuclear Thermal Propulsion manager. The lead author was the task manager of the Multiphysics Thrust Chamber Modeling task, and Ron Litchford was the task manager of the Hot-Hydrogen Materials and Component Development task. Thermal properties provided by Panda Binayak, Robert Hickman, and Bill Emrich are acknowledged.

References

[1] Howe, S. D., "Identification of Archived Design Information for Small Class Nuclear Rockets," 41st AIAA/ASME/SAE/ASEE Joint Propulsion Conference, AIAA Paper 2005-3762, 2005.

[2] Bordelon, W. J., Ballard, R. O., and Gerrish, H. P., Jr., "A Programmatic and Engineering Approach to the Development of a Nuclear Thermal Rocket for Space Exploration," AIAA Paper 2006–5082, July 2006.

[3] Lyon, L. L., "Performance of (U,Zr)C-Graphite (Composite) and of (U, Zr)C (Carbide) Fuel Elements in the Nuclear Furnace 1 Test Reactor," Los Alamos Scientific Laboratory LA-5398-MS, Los Alamos, NM, 1973.

[4] Litchford, R. J., Foote, J. P., Wang, T.-S., Hickman, R., Panda, B., Dobson, C., Osborne, R., and Clifton, C., "Arc-Heater Facility for Hot Hydrogen Exposure of Nuclear Thermal Rocket materials," 42nd AIAA/ASME/SAE/ASEE Joint Propulsion Conference, AIAA Paper 2006-5083, 2006.

[5] Shang, H. M., and Chen, Y.-S., "Unstructured Adaptive Grid Method for Reacting Flow Computation," AIAA Paper 1997–3183, July 1997.

[6] Chang, G., Ito, Y., Ross, D., Chen, Y.-S., Zhang, S., and Wang, T.-S., "Numerical Simulations of Single Flow Element in a Nuclear Thermal Thrust Chamber," AIAA Paper 2007–4143, June 2007.

[7] Wang, T.-S., Chen, Y.-S., Liu, J., Myrabo, L. N., and Mead, F. B., Jr., "Advanced Performance Modeling of Experimental Laser Lightcraft," *Journal of Propulsion and Power*, Vol. 18, No. 6, 2002, pp. 1129–1138. doi:10.2514/2.6054

[8] Wang, T.-S., "Multidimensional Unstructured-Grid Liquid Rocket Engine Nozzle Performance and Heat Transfer Analysis," *Journal of Propulsion and Power*, Vol. 22, No. 1, 2006, pp. 78–84. doi:10.2514/1.14699

[9] Wang, T.-S., "Transient Three-Dimensional Startup Side Load Analysis of a Regeneratively Cooled Nozzle," *Shock Waves*, Vol. 19, No. 3, 2009, pp. 251–264. doi:10.1007/s00193-009-0201-2

[10] Chen, Y.-S., and Kim, S. W., "Computation of Turbulent Flows Using an Extended k–ε Turbulence Closure Model," NASA CR-179204, 1987.

[11] Wang, T.-S., "Thermophysics Characterization of Kerosene Combustion," *Journal of Thermophysics and Heat Transfer*, Vol. 15, No. 2, 2001, pp. 140–147. doi:10.2514/2.6602

[12] Wang, T.-S., Droege, A., D'Agostino, M., Lee, Y.-C., and Williams, R., "Asymmetric Base-Bleed Effect on Aerospike Plume-Induced Base-Heating Environment," *Journal of Propulsion and Power*, Vol. 20, No. 3, 2004, pp. 385–393. doi:10.2514/1.10385

[13] Wang, T.-S., Foote, J., and Litchford, R., "Multiphysics Thermal-Fluid Design Analysis of a Non-Nuclear Tester for Hot-Hydrogen Material Development," *Space Technology and Applications International Forum (STAIF-2006)*, edited by M. S. El-Genk, and N. Y. Melville, Vol. 813, American Institute of Physics Proceedings, Albuquerque, NM, 12–16 Feb. 2006, pp. 537–544.

[14] Steinbrenner, J. P., Chawner, J. R., and Fouts, C., "Multiple Block Grid Generation in the Interactive Environment," AIAA Paper 90-1602, June 1990.

[15] Gaski, J., "The Systems Improved Numerical Differencing Analyzer (SINDA) Code: a User's Manual," Aerospace Corp., El Segundo, CA, Feb. 1986.